Designing Surface-Functionalized $Ti_3C_2T_2$-$Cs_3Bi_2Br_9$ (T=O, Cl, OH, or F) Heterostructures for Perovskite Optoelectronic Applications

Biao Liu,[1] Xiangxiang Feng,[1] Mengqiu Long,[1] Meng-Qiu Cai,[2] and Junliang Yang[1,*,†]

[1] *Hunan Key Laboratory for Super-microstructure and Ultrafast Process, School of Physics and Electronics, Central South University, Changsha 410083, Hunan, China*

[2] *School of Physics and Electronics Science, Hunan University, Changsha 410082, Hunan, China*

(Received 4 March 2022; revised 7 October 2022; accepted 7 October 2022; published 14 November 2022)

*MX*ene has emerged as one of the frontier two-dimensional materials. In this work, $Ti_3C_2T_2$($T = -O, -Cl, -OH$, or $-F$) *MX*ene-$Cs_3Bi_2Br_9$ perovskite heterostructures are constructed, and the various surface terminations of $Ti_3C_2T_2$ can achieve functionalized perovskite optoelectronic applications in the heterostructures. Lattice-mismatch rates of the $Ti_3C_2T_2$ and $Cs_3Bi_2Br_9$ heterostructures are only about 1%, which makes the electronic properties of $Cs_3Bi_2Br_9$ independent of lattice stress in the heterostructures. The binding energies of the $Ti_3C_2T_2/Cs_3Bi_2Br_9$ interfaces are quite low, especially at the $Ti_3C_2(OH)_2/Cs_3Bi_2Br_9$ interface. Due to the adjustable work function (WF) of $Ti_3C_2T_2$, the types of interface contacts are different, including n- and p-type Schottky contacts and an ohmic contact. The $Ti_3C_2(OH)_2/Cs_3Bi_2Br_9$ interface is an ohmic contact; this is attributed to the big difference in the WFs of $Ti_3C_2(OH)_2$ and $Cs_3Bi_2Br_9$, which could greatly boost the charge-carrier separation and transfer efficiency. In addition, the constructed heterostructures enhance the optical absorption coefficient and reduce charge-carrier effective masses. These results indicate that the $Ti_3C_2T_2/Cs_3Bi_2Br_9$ heterostructures, especially $Ti_3C_2(OH)_2/Cs_3Bi_2Br_9$, can significantly improve the optoelectronic performance of the lead-free perovskite.

DOI: 10.1103/PhysRevApplied.18.054036

I. INTRODUCTION

With an emphasis on clean and renewable energy resources, a great deal of research has focused on high-efficiency optoelectronic materials. *MX*enes are a recently discovered large family of two-dimensional (2D) layered carbide and nitride transition metals reported by the Gogotsi group in 2011, which have been extensively investigated in various fields, including energy storage, catalysis, electromagnetic applications, light-emitting diodes, sensors, water purification, and biomedical fields, that exhibit promising applications in photoelectric devices [1–3]. Among various *MX*enes, $Ti_3C_2T_2$ (T represents various surface terminations, for example, -O, -Cl, -OH, and -F) possesses high electrical conductivity and carrier mobility, excellent mechanical strength, good thermal conductivity, excellent transparency, and a tunable work function (WF) [4–6]. All these characteristics make $Ti_3C_2T_2$ suitable for electrodes in optoelectronic devices [7–9].

In recent years, halide perovskites with the formula $A_3B_2X_9$($A = \mathrm{Cs or Rb}, B = \mathrm{Sb or Bi}, \mathrm{and} X = \mathrm{halogen}$) have been at the forefront of research due to their potential applications in optoelectronic devices and are frequently employed as photocatalysts for a wide spectrum of reactions [10–12]. Since the toxicity of lead is a consistent concern for environmental and health safety, lead-free halide perovskites have great importance. Among several important materials under study, all-inorganic lead-free cesium bismuth halide, $Cs_3Bi_2Br_9$, has emerged as a typical representative for comprehensive research, as it is found to be stable under atmospheric conditions [13,14]. However, due to the poor carrier separation and transport efficiency of $Cs_3Bi_2Br_9$, its photocatalytic performance has not been very good so far. The main aspects to improve the photocatalytic performance of materials include strengthening visible-light adsorption, enhancing the separation efficiency of photogenerated electron-hole pairs, and reducing charge recombination. Numerous studies have revealed that building perovskite heterostructures can lead to some incredible properties to greatly improve their photocatalytic and optoelectronic performances [15,16]. For example, the $CsPbI_3$/PbSe heterostructure not only improves the absorption of sunlight but also passivates the surface of perovskite, which results in a lower trap density and prolonged exciton lifetime [17].

The layered characteristics of 2D $Ti_3C_2T_2$ *MX*enes make them a highly compatible material to accommodate

*412401908@qq.com
†junliang.yang@csu.edu.cn

a secondary material to build heterostructures that can integrate the original excellent electronic properties of the isolated components and create particularly advantageous performances. Furthermore, the $Ti_3C_2T_2$ *MX*enes can be used directly as an electrode material in various photoelectric devices to improve the performance [18–22]. For example, $Ti_3C_2T_x$ *MX*ene materials as electrodes in a 2D $CsPbBr_3$ photodetector exhibit an outstanding *on*:*off* current ratio up to 2.3×10^3 and a remarkable photoresponse as fast as 18 ms. However, the interface characteristics and transport mechanisms resulting from the various surface terminations of 2D $Ti_3C_2T_2$ in the heterostructures are unclear.

Herein, heterostructures of lead-free $Cs_3Bi_2Br_9$ perovskite and 2D $Ti_3C_2T_2$ are built. The structures and interfacial electronic properties of the heterojunctions are systematically and comprehensively studied by first-principles methods. Due to various surface terminations of $Ti_3C_2T_2$, the visible-light adsorption, interface charge-transport characteristics, and separation efficiency are different. Therefore, lead-free $Cs_3Bi_2Br_9$ perovskite devices can be regulated by the differentiation of the $Ti_3C_2T_2$ surface terminations to improve the device performances.

II. METHODS

All of the results are calculated by using the Vienna *ab initio* simulation package code, based on density-functional theory (DFT) [23–25]. The projector-augmented wave method is used to describe the interaction between the ion cores and valence electrons. The Perdew-Burke-Ernzerhof (PBE) functional combined with the DFT-D3 method is used for structural optimization [26]. The PBE functional and hybrid exchange-correlation functional (HSE06) are both used for comparison to study the electronic properties [27]. A mesh of $4 \times 4 \times 1$ k points is adopted for structure optimization and electronic property calculations. The cutoff energy is 450 eV in the calculations. The convergence criteria for the energy and atomic Hellmann-Feynman forces is 1×10^{-4} eV and 0.02 eV/Å, respectively.

III. RESULTS

The relaxed lattice parameters of $Cs_3Bi_2Br_9$ bulk are $a = b = 8.214$ Å and $c = 10.068$ Å, which are consistent with experimental results ($a = b = 8.216$ and $c = 10.07$ Å) [28]. The calculated lattice parameters of $Ti_3C_2T_2$ are from 3.01 to 3.14 Å for various surface terminations, -O, -Cl, -OH, and -F, which are similar to experimental or theoretical values. It is well known that the HSE06 functional is very often more reliable for solids [29,30]. The band structures of $Cs_3Bi_2Br_9$ bulk are calculated by using the PBE functional and HSE06 functional, as seen in Fig. S1 within the Supplemental Material [45]. The band gaps of the $Cs_3Bi_2Br_9$ bulk are 2.595 and 3.252 eV from the PBE and HSE06 functionals, respectively. However, the band gap of the $Cs_3Bi_2Br_9$ bulk is 2.7 eV in experiments [10]. Therefore, it is more reasonable to use the PBE functional to calculate the electronic properties of $Cs_3Bi_2Br_9$ perovskite. The calculated band structures of $Ti_3C_2T_2$ monolayers reveal that they show metallic properties. They have high electrical conductivity, high transparency, and outstanding flexibility [22]. Therefore, all these properties make $Ti_3C_2T_2$ suitable for electrodes in optoelectronic devices.

$Ti_3C_2T_2$ is a monolayer structure that can be used to construct heterostructures by stacking directly. However, $Cs_3Bi_2Br_9$ is a bulk structure and has different surfaces. Three surface models are constructed and depicted in Fig. S2 within the Supplemental Material [45]. The surface energy can determine the stability of a surface. The surface energy is calculated by [31,32]

$$\gamma = \frac{1}{2A}[E_{\text{slab}} - nE_{\text{bulk}}],$$

where A is the surface area, E_{slab} is the energy of the surface model, E_{bulk} is the energy of $Cs_3Bi_2Br_9$ bulk, and n is the number of bulk repeating units in the surface model. n is usually equal to three and many calculations support this conclusion [33,34]. The calculated surface energies are given in Table S1 within the Supplemental Material [45]. The smaller the surface energy, the more stable the surface. When the surface energy is as low as 20 meV/Å^2, the energy falls very close to the exfoliation energy of the compound [31,32]. Therefore, the $CsBr_2$ surface is most stable and this can be attributed to van der Waals interactions. When setting the vacuum energy level to zero, the calculated conduction-band minimum, valence-band maximum, and Fermi level of the $CsBr_2$ surface are −3.94, −6.58, and −6.32 eV, respectively. The band-gap value (2.641 eV) is equivalent to the calculated value of the $Cs_3Bi_2Br_9$ bulk. Therefore, the $CsBr_2$ surface can be used to construct heterostructures.

The $Ti_3C_2T_2/Cs_3Bi_2Br_9$ heterostructures are constructed from a 1×1 001 $Cs_3Bi_2Br_9$ surface and 2×2 (rotation between surfaces is 19°) $Ti_3C_2T_2$ monolayer. Rotation between the two layers reduces lattice strain. Three repeating octahedral units of the $Cs_3Bi_2Br_9$ are applied in the heterostructure, which has a similar performance to that of the bulk material [35]. Four representative surface terminations (-O, -Cl, -OH, and -F) of $Ti_3C_2T_2$ are selected. The Ti_3C_2 monolayer without surface termination is also used to construct a heterostructure for comparison. The relaxed configuration diagrams are shown in Fig. 1. A 15-Å vacuum region is set to avoid repeated interactions in the Z direction. The lattice mismatches of the 1×1 $Cs_3Bi_2Br_9$ and 2×2 $Ti_3C_2T_2$ monolayers are quite small and only about 1% in the heterostructures; thus, the electronic properties of $Cs_3Bi_2Br_9$ are independent of lattice stress. The vertical interlamellar spacing and minimum

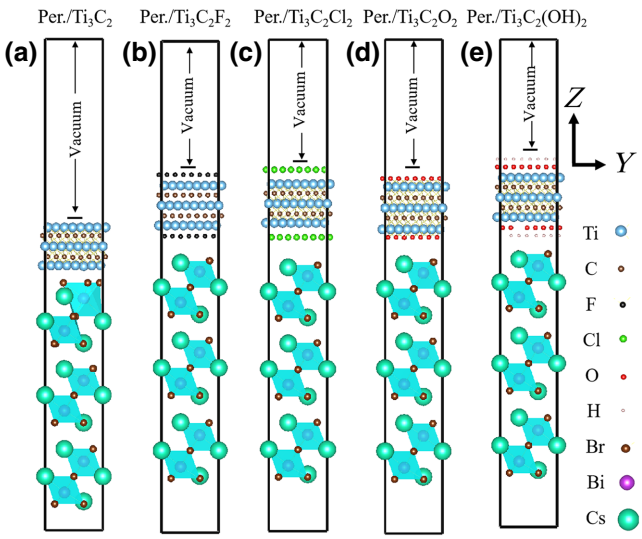

FIG. 1. Relaxed heterostructure configurations of (a) $Cs_3Bi_2Br_9/Ti_3C_2$, (b) $Cs_3Bi_2Br_9/Ti_3C_2F_2$, (c) $Cs_3Bi_2Br_9/Ti_3C_2Cl_2$, (d) $Cs_3Bi_2Br_9/Ti_3C_2O_2$, (e) $Cs_3Bi_2Br_9/Ti_3C_2(OH)_2$. Vacuum region is over 15 Å in the Z direction. These configurations are drawn to scale.

interface-bonding distance of the $Cs_3Bi_2Br_9/Ti_3C_2T_2$ heterostructures are calculated and given in Table S2 within the Supplemental Material [45]. The minimum interface-bonding distance of the various surface terminations and $Cs_3Bi_2Br_9$ are over 2.5 Å. The interface-binding energies are calculated to determine how easy it is to form the interface. The formula for calculating the binding energies is [36]

$$E_b = E_{\text{het.}} - E_{\text{Ti}_3\text{C}_2T_2} - E_{\text{Cs}_3\text{Bi}_2\text{Br}_9},$$

where $E_{\text{het.}}$, $E_{\text{Ti}_3\text{C}_2T_2}$, and $E_{\text{Cs}_3\text{Bi}_2\text{Br}_9}$ are the energies of the heterostructure, $Ti_3C_2T_2$ monolayer, and $Cs_3Bi_2Br_9$, respectively. The lower the binding energy, the easier it is to form the heterostructure. Binding-energy data are given in Table S3 within the Supplemental Material [45]. The results show that all of the energies are very low, especially the $Ti_3C_2(OH)_2/Cs_3Bi_2Br_9$ heterostructure, which has a negative value. Therefore, the $Ti_3C_2(OH)_2/Cs_3Bi_2Br_9$ heterostructure can likely be easily formed, in theory.

The band-structure diagram can directly reflect the interface electronic properties of the heterostructure. The band-structure schemes of $Cs_3Bi_2Br_9/Ti_3C_2T_2$ heterostructures are shown in Fig. 2. The energy-level diagrams of $Cs_3Bi_2Br_9$ and $Ti_3C_2T_2$ in the precontact states are given in Fig. S3 within the Supplemental Material [45] to facilitate a comparison of energy-level transitions. The results show that the interfaces between $Cs_3Bi_2Br_9$ and $Ti_3C_2T_2$ are metal-semiconductor contacts. The contacting types of heterostructures include n- and p-type Schottky contacts and an ohmic contact. As shown in Fig. 2, the shapes of the $Cs_3Bi_2Br_9$ bands in the heterostructure are very similar to the bulk, and the band gaps in the heterostructures are close to the bulk, as listed in Table I. These results indicate that the excellent properties of the $Cs_3Bi_2Br_9$ perovskite are not destroyed in the heterostructures. Experimental results show that 2D $Ti_3C_2T_2$ MXene nanosheets accelerate the separation and transfer efficiency of electron-hole pairs and simultaneously suppress their recombination, resulting in improved utilization of the excited charges, which account for the highly enhanced photocatalytic performance [37]. In fact, contact types are abundant in the $Cs_3Bi_2Br_9/Ti_3C_2T_2$ heterostructures and the transfer of interface electrons is inconsistent. The $Cs_3Bi_2Br_9/Ti_3C_2$ and $Cs_3Bi_2Br_9/Ti_3C_2Cl_2$ heterostructures are n-type Schottky contacts and the barrier heights are 0.69 and 0.85 eV, respectively. The $Cs_3Bi_2Br_9/Ti_3C_2F_2$ and $Cs_3Bi_2Br_9/Ti_3C_2O_2$ heterostructures are p-type Schottky contacts and the barrier heights are 0.54 and 0.48 eV, respectively. The $Cs_3Bi_2Br_9/Ti_3C_2(OH)_2$ heterostructure is an ohmic contact and the barrier height is

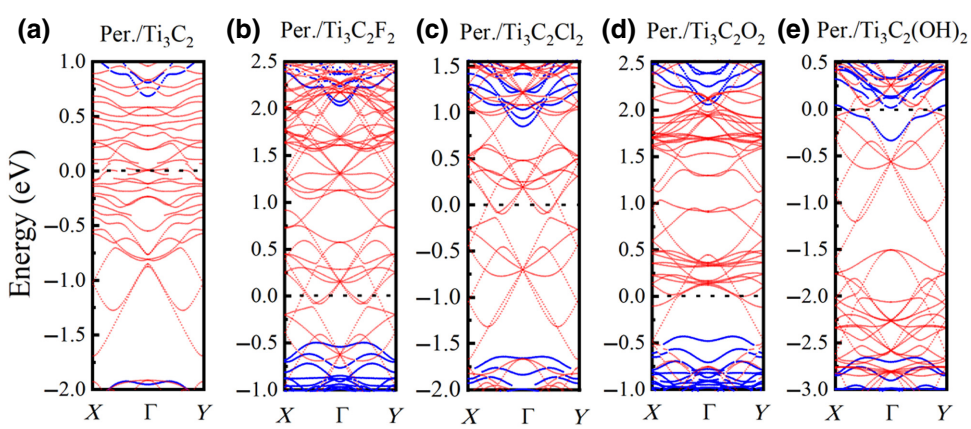

FIG. 2. Band structures of (a) $Cs_3Bi_2Br_9/Ti_3C_2$, (b) $Cs_3Bi_2Br_9/Ti_3C_2F_2$, (c) $Cs_3Bi_2Br_9/Ti_3C_2Cl_2$, (d) $Cs_3Bi_2Br_9/Ti_3C_2O_2$, (e) $Cs_3Bi_2Br_9/Ti_3C_2(OH)_2$ heterostructures. Blue and red lines denote the contributions from $Cs_3Bi_2Br_9$ and $Ti_3C_2T_2$, respectively. Fermi level is set at zero.

TABLE I. Band gaps, contact type, and barrier heights of the $Cs_3Bi_2Br_9/Ti_3C_2$, $Cs_3Bi_2Br_9/Ti_3C_2F_2$, $Cs_3Bi_2Br_9/Ti_3C_2Cl_2$, $Cs_3Bi_2Br_9/Ti_3C_2O_2$, and $Cs_3Bi_2Br_9/Ti3C_2(OH)_2$ heterostructures.

	$Cs_3Bi_2Br_9/Ti_3C_2$	$Cs_3Bi_2Br_9/Ti_3C_2F_2$	$Cs_3Bi_2Br_9/Ti_3C_2Cl_2$	$Cs_3Bi_2Br_9/Ti_3C_2O_2$	$Cs_3Bi_2Br_9/Ti_3C_2(OH)_2$
Band gap (eV)	2.64	2.57	2.51	2.54	2.32
Contact type	*n*	*p*	*n*	*p*	ohmic contact
Barrier height (eV)	0.69	0.54	0.85	0.48	0

zero. Therefore, electrons are more easily separated and diffuse in the $Cs_3Bi_2Br_9/Ti_3C_2(OH)_2$ heterostructure than other $Cs_3Bi_2Br_9/Ti_3C_2T_2$ heterostructures.

The WF difference drives electrons and holes to move spontaneously. The vacuum levels, Fermi levels, and WFs of $Cs_3Bi_2Br_9$ and $Ti_3C_2T_2$ are listed in Table II. The change of the work function induced by the functional group can be given by [38–40]

$$\emptyset - \emptyset_0 = -\frac{e}{\varepsilon_0}[\Delta P + (P_s - P_0)],$$

where $\emptyset$ and $\emptyset_0$ are the WFs of $Ti_3C_2T_2$ and Ti_3C_2, and ΔP, P_s, and P_0 are the change of the dipole density, the surface dipole density of the Ti_3C_2 substrate, and the surface dipole density of the clean Ti_3C_2 surface (fully relaxed), respectively. The change of the dipole density of the surface functional group is given by [38]

$$\Delta P(z) = \int_0^z z\Delta\rho(z)dz,$$

where $\Delta\rho$ is the change of charge density of the surface-functional-group-covered Ti_3C_2 surface. There are two contributions to the change of the WF. The first is a charge-rearrangement effect, which is contributed to by charge transfer due to the difference in electronegativity and hybridization between the surface-functional-group layer and the substrate, as given by ΔP. The second contribution is due to the relaxation of the substrate induced by the overlayer, given by $(P_s - P_0)$, and the $(P_s - P_0)$ term is usually smaller than the ΔP term. In general, if the surface functional group is more electronegative than the substrate (Ti_3C_2), electrons will be transferred to the surface-functional-group layer, causing an excess of negative charges on the outside and an excess of positive charges on the inside of the surface. This leads to a negative dipole that reinforces the original surface dipole due to electron "spill out," causing the work function to increase. The surface functional groups (-F, -Cl, -O, and -OH) in $Ti_3C_2T_2$ are more electronegative than the Ti_3C_2 substrate, but the calculated WF of $Ti_3C_2(OH)_2$ decreases. The change of charge density and the dipole density of the surface-functional-group-covered Ti_3C_2 surface are shown in Fig. 3. It is shown that the electrons are transferred from Ti_3C_2 to the surface functional groups, which is consistent with electronegativity. Due to the rearrangement of electronic charge density in the surface-functional-group layer to form chemical bonding in the interface, there is also a depletion of electrons in the outer "tail" region

TABLE II. Vacuum levels, Fermi levels, and work functions of $Ti_3C_2T_2$ and $Cs_3Bi_2Br_9$.

Type	E_v	E_F	WF
Ti_3C_2	2.94	−1.33	4.27
$Ti_3C_2F_2$	4.30	−1.40	5.70
$Ti_3C_2Cl_2$	4.97	0.23	4.74
$Ti_3C_2O_2$	4.43	−1.83	6.26
$Ti_3C_2(OH)_2$	2.94	1.36	1.58
$Cs_3Bi_2Br_9$	3.15	−3.17	6.32

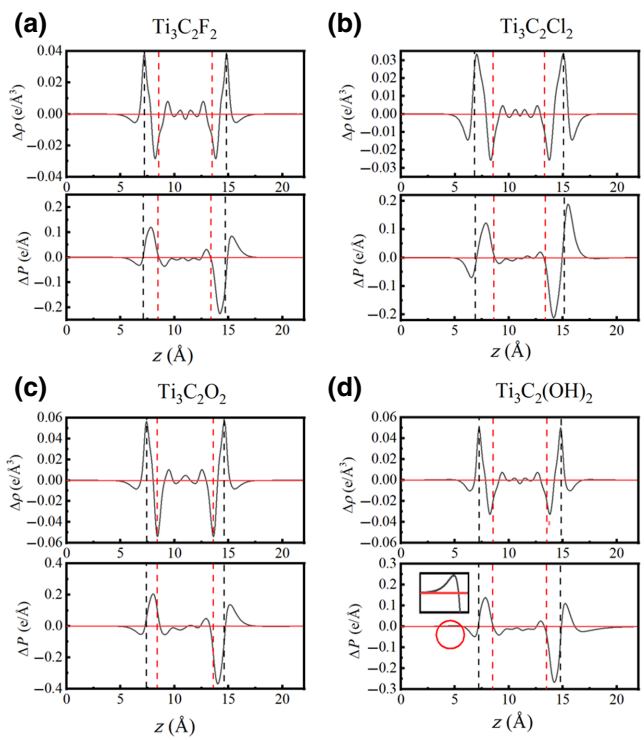

FIG. 3. Change of charge density and dipole density of (a) $Ti_3C_2F_2$, (b) $Ti_3C_2Cl_2$, (c) $Ti_3C_2O_2$, and (d) $Ti_3C_2(OH)_2$. The *x*-axis coordinates represent the *z* position (Å). Red dotted vertical line represents the position of *Z* direction in Ti_3C_2 and black dotted vertical line represents the position of the surface functional group. Negative value of $\Delta\rho$ means a depletion of electrons, and positive value means an excess of electrons.

of the surface-functional-group layer. The number of electrons outside the surface-functional-group area is small, so it will not affect the sign of charge transfer. However, the dipole is weighted by the distance "z;" this can have important consequences on the sign of ΔP. When the value of ΔP in the outer tail region is negative, the WF increases. However, the depletion of electrons in the outer tail region gives a positive contribution to ΔP. Although the amount of charge in the outer tail region is small, the weighting by z in the integral may be sufficient to turn the sign of ΔP from negative to positive, which then makes the WF decrease. As shown in Fig. 3(d), the sign of ΔP is positive and the WF of $Ti_3C_2(OH)_2$ is less than that of Ti_3C_2.

Charge transfer can be indicated by the difference in WF. The WF of $Cs_3Bi_2Br_9$ is bigger than all of those of $Ti_3C_2T_2$. $Cs_3Bi_2Br_9$ is also a p-type semiconductor, as seen in Figs. S1 and S4 within the Supplemental Material [45]. Generally speaking, when $Cs_3Bi_2Br_9$ and $Ti_3C_2T_2$ are in contact, the electrons spontaneously move from the high-Fermi-level $Ti_3C_2T_2$ part to the low-Fermi-level $Cs_3Bi_2Br_9$ part until all Fermi levels reach the same height in the metal-semiconductor heterostructures. Spontaneous electron movement leads to the $Ti_3C_2T_2$ electric potential rising and the Fermi level lowering in the heterostructures. The holes of $Cs_3Bi_2Br_9$ spontaneously move from $Cs_3Bi_2Br_9$ to $Ti_3C_2T_2$. The interface band edges of $Cs_3Bi_2Br_9$ will bend down in the heterostructures. For the p-type $Cs_3Bi_2Br_9$ semiconductor, the bending-down band edge will result in the aggregation of holes at the interface and the formation of a p-type barrier layer. Due to the WF difference of $Cs_3Bi_2Br_9$ and $Ti_3C_2(OH)_2$ being much greater than the band gap of $Cs_3Bi_2Br_9$, a large number of electrons fill $Cs_3Bi_2Br_9$, and the Fermi level of $Cs_3Bi_2Br_9$ is pushed up so much that it goes beyond the conduction-band minimum, which results in the ohmic contact in the $Cs_3Bi_2Br_9/Ti_3C_2(OH)_2$ heterostructure. For the $Cs_3Bi_2Br_9/Ti_3C_2F_2$ and $Cs_3Bi_2Br_9/Ti_3C_2O_2$ heterostructures, the WF difference between $Cs_3Bi_2Br_9$ and $Ti_3C_2F_2$ or $Ti_3C_2O_2$ is small, so the Fermi level of $Cs_3Bi_2Br_9$ is only pushed up a little. Therefore, they are p-type Schottky contacts. For the $Cs_3Bi_2Br_9/Ti_3C_2$ and $Cs_3Bi_2Br_9/Ti_3C_2Cl_2$ heterostructures, their WF differences are more than half the band gap but less than the band gap of $Cs_3Bi_2Br_9$; therefore, they show n-type Schottky contacts. In fact, charge transfer is related not only to the difference in the WF but also to interface-induced states inside the gap of semiconductors [41].

The plane-averaged charge-density difference, $\Delta\rho$, can be used to reveal the nature of the transport characteristics at the heterostructure interface. $\Delta\rho$ along the z direction, $\Delta\rho(z)$, can be calculated by [34]

$$\Delta\rho(z) = \rho_{\text{het.}} - \rho_{Ti_3C_2T_2} - \rho_{Cs_3Bi_2Br_9},$$

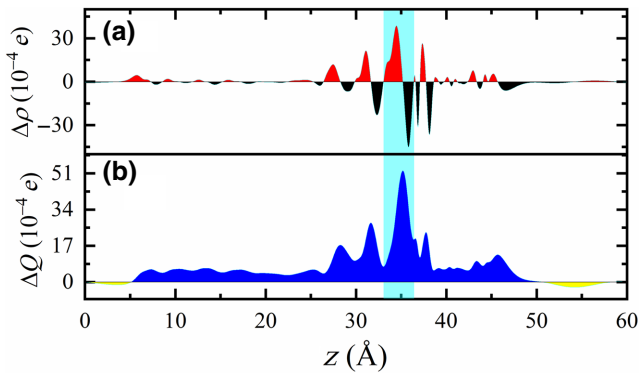

FIG. 4. (a) z-Direction plane-averaged charge-density difference, $\Delta\rho(z)$, of $Cs_3Bi_2Br_9/Ti_3C_2(OH)_2$ heterostructure. Red and black areas represent electron accumulation and depletion, respectively. (b) z-Direction charge-displacement curve of $Cs_3Bi_2Br_9/Ti_3C_2(OH)_2$ heterostructure. Blue and yellow areas represent positive and negative values, respectively. Light-blue bar indicates the interface. x-Axis is in angstrom.

where $\rho_{\text{het.}}$ is the plane-averaged density of the heterostructure. $\rho_{Ti_3C_2T_2}$ and $\rho_{Cs_3Bi_2Br_9}$ are the plane-averaged densities of the $Ti_3C_2T_2$ monolayer and $Cs_3Bi_2Br_9$ slabs, respectively. Due to the ohmic contact characteristics of the $Cs_3Bi_2Br_9/Ti_3C_2(OH)_2$ heterostructure, $\Delta\rho(z)$ of the $Cs_3Bi_2Br_9/Ti_3C_2(OH)_2$ heterostructure is plotted as the key research object, as shown in Fig. 4(a), which can describe the interfacial charge-transport mechanism quantitatively. The whole heterostructure system is neutral. When r is sufficiently far from the heterostructure interface, $\Delta\rho(z)$ becomes closer to zero. The positive and negative signs of $\Delta\rho(z)$, respectively, denote charge accumulation and depletion, and two colors (red and black) are used to distinguish the difference between accumulation and depletion. It is obvious from Fig. 4(a) that the main peaks of charge accumulation (red) and depletion (black) occur in the interface region, and some secondary peaks occur inside the $Cs_3Bi_2Br_9$ and $Ti_3C_2(OH)_2$ monolayers. The peaks are due to interfacial hybridization of the electronic states between MXene and perovskite. The density of states of Bi, Br, and Ti atoms are calculated and prove interface hybridization, as seen in Fig. S5 within the Supplemental Material [45]. The interface hybridization will form a dipole at the interface. Therefore, the main dipole is generated between the $Cs_3Bi_2Br_9$ and $Ti_3C_2(OH)_2$ interface. The dipole is derived from interfacial polarization. Polarization at the interface will promote charge separation and transfer. These secondary peaks occurring inside the $Cs_3Bi_2Br_9$ and $Ti_3C_2(OH)_2$ monolayers may lead to different dipole directions in the heterostructure, but the overall direction of polarization in the heterostructure can be determined by the charge-displacement function, ΔQ. ΔQ can

be obtained by integrating $\Delta\rho(z)$ along the z direction [42]:

$$\Delta Q = \int_0^z \Delta\rho dz.$$

Positive ΔQ denotes net charge transfer along the opposite $-z$ direction, and a negative value indicates charge flow along the z direction. The ΔQ values of the $Cs_3Bi_2Br_9/Ti_3C_2(OH)_2$ heterostructure are shown in Fig. 4(b). It is noted that the positive ΔQ value on the perovskite side indicates charge transfer from the $Ti_3C_2(OH)_2$ monolayer to the $Cs_3Bi_2Br_9$ perovskite side. A large number of electrons fill the $Cs_3Bi_2Br_9$ perovskite, causing the Fermi level to rise sharply beyond the conduction-band minimum. Therefore, the heterostructure forms a stable ohmic contact. ΔQ values of other heterostructures are given in Fig. S6 within the Supplemental Material [45]. The polarization direction or Schottky barrier at the interface reduces the efficiency of interface charge separation and diffusion in the other heterostructures. In $Cs_3Bi_2Br_9/Ti_3C_2$ and $Cs_3Bi_2Br_9/Ti_3C_2F_2$, ΔQ is continuously positive, which indicates that the polarization direction is along the $-z$ direction. The inner charge of the perovskite that is transported and diffused out needs to overcome not only the Schottky barrier but also the dipole barrier. In $Cs_3Bi_2Br_9/Ti_3C_2Cl_2$ and $Cs_3Bi_2Br_9/Ti_3C_2O_2$, ΔQ is continuously negative and the polarization direction is along the z direction. Although the inner charges of the perovskite that are transported and diffused out do not need overcome the obstacle of a dipole, the Schottky barrier still needs to be overcome. Moreover, the direction of charge transfer is inconsistent with the difference in WFs; this could be because of the interface-induced states inside the gap of $Cs_3Bi_2Br_9$ [41].

The optical absorption coefficient is calculated to study the optical properties of the $Cs_3Bi_2Br_9/Ti_3C_2T_2$ heterostructures [43]:

$$\alpha = \left(\sqrt{2}\right)\omega\left[\sqrt{\varepsilon_1(\omega)^2 + \varepsilon_2(\omega)^2} - \varepsilon_1(\omega)\right]^{1/2},$$

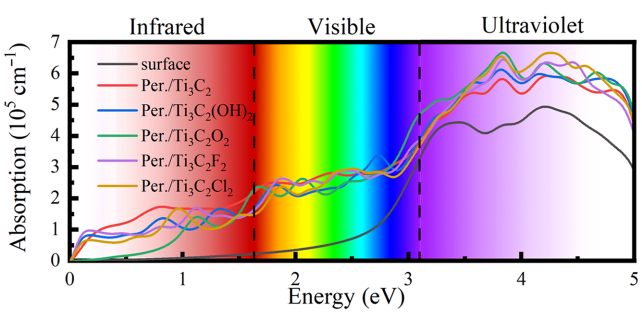

FIG. 5. Absorption spectra of the $Cs_3Bi_2Br_9$ surface and $Cs_3Bi_2Br_9/Ti_3C_2T_2$ heterostructures.

TABLE III. Effective masses of the surface of $Cs_3Bi_2Br_9$ and heterostructures of $Cs_3Bi_2Br_9/Ti_3C_2$, $Cs_3Bi_2Br_9/Ti_3C_2F_2$, $Cs_3Bi_2Br_9/Ti_3C_2Cl_2$, $Cs_3Bi_2Br_9/Ti_3C_2O_2$, and $Cs_3Bi_2Br_9/Ti_3C_2(OH)_2$ along x and y directions.

	Electron		Hole	
Effective mass (m_0)	m_x^*	m_y^*	m_x^*	m_y^*
$Cs_3Bi_2Br_9$ surface	0.67	0.67	5.27	5.27
$Cs_3Bi_2Br_9/Ti_3C_2$	0.66	0.70	3.57	3.82
$Cs_3Bi_2Br_9/Ti_3C_2F_2$	0.68	0.98	1.79	1.95
$Cs_3Bi_2Br_9/Ti_3C_2Cl_2$	0.71	0.71	4.48	4.48
$Cs_3Bi_2Br_9/Ti_3C_2O_2$	0.69	0.67	2.44	2.44
$Cs_3Bi_2Br_9/Ti_3C_2(OH)_2$	0.66	0.67	2.10	2.17

where α is the absorption coefficient; $\varepsilon_1(\omega)$ and $\varepsilon_2(\omega)$ are the real and imaginary parts of the dielectric function, respectively, which depends on the optical frequency, ω. The calculated optical absorption spectra of the $Cs_3Bi_2Br_9/Ti_3C_2T_2$ heterostructures and $Cs_3Bi_2Br_9$ surface are shown in Fig. 5. Compared to the $Cs_3Bi_2Br_9$ surface, the optical absorption coefficient is enhanced in the heterostructures, especially in the visible-light range. These results are also confirmed experimentally [37]. Therefore, the light-absorption coefficient of $Cs_3Bi_2Br_9$ slabs can be improved by building $Cs_3Bi_2Br_9/Ti_3C_2T_2$ heterostructures.

The effective masses (m^*) can be used to illustrate the carrier-transport properties. The effective masses are calculated by [44]

$$m_i^* = \hbar^2\left[\frac{\partial^2\varepsilon(k)}{\partial k^2}\right]^{-1},$$

where the k is the wave-vector directions and $\varepsilon(k)$ represents the eigenvalues of the energy band. m_x^* and m_y^* represent Γ-X and Γ-Y directions, respectively. The calculated effective masses of the $Cs_3Bi_2Br_9$ surface and $Cs_3Bi_2Br_9$ part of the $Cs_3Bi_2Br_9/Ti_3C_2T_2$ heterostructures are listed in Table III. The results show that the effective mass of electrons is smaller than that of the holes. The small effective mass of electrons is not affected by the heterostructure model, and the effective mass of holes decreases slightly in the heterostructures compared with the individual $Cs_3Bi_2Br_9$ surface. These results suggest that the constructed heterostructure will facilitate charge-carrier migration and improve the optoelectronic performance of $Cs_3Bi_2Br_9$.

IV. CONCLUSION

The structures and photoelectrical properties of $Cs_3Bi_2Br_9/Ti_3C_2T_2$ heterostructures are investigated. The lattice mismatches of one lattice of $Cs_3Bi_2Br_9$ and the $Ti_3C_2T_2$ monolayer are only about 1% in the heterostructures; this makes the electronic properties of $Cs_3Bi_2Br_9$ independent

of lattice stress. The $Cs_3Bi_2Br_9/Ti_3C_2(OH)_2$ heterostructure is an ohmic contact; this is attributed to the big difference in the WFs of $Ti_3C_2(OH)_2$ and $Cs_3Bi_2Br_9$. Although the transferred charges lead to charges accumulating at the $Cs_3Bi_2Br_9$ perovskite surface, this does not affect the free diffusion of most photon-generated carriers inside the $Cs_3Bi_2Br_9$ perovskite. In addition, the light-absorption coefficients are enhanced, and the effective masses are decreased in the $Cs_3Bi_2Br_9/Ti_3C_2T_2$ heterostructures. These results open an avenue to explore more efficient and functionalized all-inorganic lead-free perovskite photoelectric devices.

Data that support the findings of this study are available from the corresponding author upon reasonable request.

ACKNOWLEDGMENTS

The authors acknowledge support from the National Natural Science Foundation of China (Grants No. 62004225 and 52173192), the National Key Research and Development Program of China (Grant No. 2017YFA 0206600), the Science and Technology Innovation Program of Hunan Province (Grant No. 2020RC4004), and the Special Funding for the Construction of Innovative Provinces in Hunan Province (Grant No. 2020GK2024).

[1] B. C. Wyatt, A. Rosenkranz, and B. Anasori, 2D *MX* enes: Tunable mechanical and tribological properties, Adv. Mater. **33**, 2007973 (2021).

[2] Y. Wei, P. Zhang, R. A. Soomro, Q. Zhu, and B. Xu, Advances in the synthesis of 2D *MX* enes, Adv. Mater. **33**, 2103148 (2021).

[3] Y. Gogotsi and B. Anasori, The rise of *MX* enes, ACS Nano **13**, 8491 (2019).

[4] Y. Pei, X. Zhang, Z. Hui, J. Zhou, X. Huang, G. Sun, and W. Huang, $Ti_3C_2T_X$ *MX* ene for sensing applications: Recent progress, design principles, and future perspectives, ACS Nano **15**, 3996 (2021).

[5] A. V. Mohammadi, J. Rosen, and Y. Gogotsi, The world of two-dimensional carbides and nitrides (*MX* enes), Science **372**, 1165 (2021).

[6] D. H. Ho, Y. Y. Choi, S. B. Jo, J. M. Myoung, and J. H. Cho, Sensing with *MX* enes: Progress and prospects, Adv. Mater. **20**, 2005846 (2021).0935-9648

[7] L. J. Yin, Y. T. Li, X. C. Yao, Y. Z. Wang, L. Jia, Q. M. Liu, J. S. Li, Y. L. Li, and D. Y. He, *MX* enes for solar cells, Nano-Micro Lett. **13**, 1 (2021).

[8] Z. X. Liu and H. N. Alshareef, *MX* enes for optoelectronic devices, Adv. Electron. Mater. **7**, 2100295 (2021).

[9] J. X. Xu, T. Peng, X. Qin, Q. Zhang, T. Y. Liu, W. B. Dai, B. Chen, H. Z. Yu, and S. W. Shi, Recent advances in 2D *MX* enes: Preparation, intercalation and applications in flexible devices, J. Mater. Chem. A **9**, 14147 (2021).

[10] Z. Ji, Y. Liu, W. Li, C. Zhao, and W. Mai, Reducing current fluctuation of $Cs_3Bi_2Br_9$ perovskite photodetectors for diffuse reflection imaging with wide dynamic range, Sci. Bull. **65**, 1371 (2020).

[11] M. Xia, J. H. Yuan, G. Niu, X. Du, L. Yin, W. Pan, J. Luo, Z. Li, H. Zhao, and K. H. Xue, Unveiling the structural descriptor of $A_3B_2X_9$ perovskite derivatives toward x-ray detectors with low detection limit and high stability, Adv. Funct. Mater. **30**, 1910648 (2020).

[12] K. Kundu, P. Acharyya, K. Maji, R. Sasmal, S. S. Agasti, and K. Biswas, Synthesis and localized photoluminescence blinking of lead-free 2D nanostructures of $Cs_3Bi_2I_6Cl_3$ perovskite, Angew. Chem., Int. Edit. **59**, 13093 (2020).

[13] H. Lei, D. Hardy, and F. Gao, Lead-free double perovskite $Cs_2AgBiBr_6$: Fundamentals, applications, and perspectives, Adv. Funct. Mater. **31**, 2105898 (2021).

[14] L. Romani, A. Speltini, C. N. Dibenedetto, A. Listorti, F. Ambrosio, E. Mosconi, A. Simbula, M. Saba, A. Profumo, and P. Quadrelli, Experimental strategy and mechanistic view to boost the photocatalytic activity of $Cs_3Bi_2Br_9$ lead-free perovskite derivative by g-C_3N_4 composite engineering, Adv. Funct. Mater. **31**, 2104428 (2021).

[15] B. Liu, M. Q. Long, M. Q. Cai, and J. L. Yang, Interface engineering of $CsPbI_3$-black phosphorus van der Waals heterostructure, Appl. Phys. Lett. **112**, 043901 (2018).

[16] B. A. Liu, M. Q. Long, M. Q. Cai, L. M. Ding, and J. L. Yang, Interfacial charge behavior modulation in 2D/3D perovskite heterostructure for potential high-performance solar cells, Nano Energy **59**, 715 (2019).

[17] S. X. Wang, C. H. Bi, A. Portniagin, J. F. Yuan, J. J. Ning, X. F. Xiao, X. Y. Zhang, Y. Y. Li, S. V. Kershaw, J. J. Tian, and A. L. Rogach, $CsPbI_3$/PbSe heterostructured nanocrystals for high-efficiency solar cells, ACS Energy Lett. **5**, 2401 (2020).

[18] A. Agresti, A. Pazniak, S. Pescetelli, A. Di Vito, D. Rossi, A. Pecchia, M. A. D. Maur, A. Liedl, R. Larciprete, D. V. Kuznetsov, *et al.*, Titanium-carbide *MX* enes for work function and interface engineering in perovskite solar cells, Nat. Mater. **18**, 1228 (2019).

[19] D. Saranin, S. Pescetelli, A. Pazniak, D. Rossi, A. Liedl, A. Yakusheva, L. Luchnikov, D. Podgorny, P. Gostischev, S. Didenko, A. et al., Transition metal carbides (*MX* enes) for efficient NiO-based inverted perovskite solar cells, Nano Energy **82**, 105771 (2021).

[20] S. Lee, E. H. Kim, S. Yu, H. Kim, C. Park, S. W. Lee, H. Han, W. Jin, K. Lee, and C. E. Lee, Polymer-laminated $Ti_3C_2T_X$ *MX* ene electrodes for transparent and flexible field-driven electronics, ACS Nano **15**, 8940 (2021).

[21] X. Xu, Y. Chen, P. He, S. Wang, K. Ling, L. Liu, P. Lei, X. Huang, H. Zhao, and J. Cao, Wearable CNT/$Ti_3C_2T_x$ *MX* ene/PDMS composite strain sensor with enhanced stability for real-time human healthcare monitoring, Nano Res. **14**, 2875 (2021).

[22] W. Deng, H. Huang, H. Jin, W. Li, X. Chu, D. Xiong, W. Yan, F. Chun, M. Xie, and C. Luo, All-sprayed-processable, large-area, and flexible perovskite/*MX* ene-based photodetector arrays for photocommunication, Adv. Opt. Mater. **7**, 1801521 (2019).

[23] P. E. Blochl, Projector augmented-wave method, Phys. Rev. B **50**, 17953 (1994).

[24] G. Kresse and D. Joubert, From ultrasoft pseudopotentials to the projector augmented-wave method, Phys. Rev. B **59**, 1758 (1999).

[25] J. P. Perdew, K. Burke, and M. Ernzerhof, Generalized Gradient Approximation Made Simple, Phys. Rev. Lett. **77**, 3865 (1996).

[26] S. Grimme, J. Antony, S. Ehrlich, and H. Krieg, A consistent and accurate *ab initio* parametrization of density functional dispersion correction (DFT-D) for the 94 elements H-Pu, J. Chem. Phys. **132**, 154104 (2010).

[27] J. Heyd, G. E. Scuseria, and M. Ernzerhof, Hybrid functionals based on a screened Coulomb potential, J. Chem. Phys. **118**, 8207 (2003).

[28] M. Gao, C. Zhang, L. Lian, J. Guo, Y. Xia, F. Pan, X. Su, J. Zhang, H. Li, and D. Zhang, Controlled synthesis and photostability of blue emitting $Cs_3Bi_2Br_9$ perovskite nanocrystals by employing weak polar solvents at room temperature, J. Mater. Chem. C **7**, 3688 (2019).

[29] T. Das, G. Di Liberto, S. Tosoni, and G. Pacchioni, Band gap of 3D metal oxides and quasi-2D materials from hybrid density functional theory: Are dielectric-dependent functionals superior?, J. Chem. Theory Comput. **15**, 6294 (2019).

[30] J. Heyd, J. E. Peralta, G. E. Scuseria, and R. L. Martin, Energy band gaps and lattice parameters evaluated with the Heyd-Scuseria-Ernzerhof screened hybrid functional, J. Chem. Phys. **123**, 174101 (2005).

[31] T. Björkman, A. Gulans, A. V. Krasheninnikov, and R. M. Nieminen, van der Waals Bonding in Layered Compounds from Advanced Density-Functional First-Principles Calculations, Phys. Rev. Lett. **108**, 235502 (2012).

[32] I.-H. Lee, D. Van Dao, G. Di Liberto, D.-Y. Shin, H. Ko, J. Park, W. Wang, Q. Van Le, T. Van Nguyen, and G. Pacchioni, $LaFeO_3$ meets nitrogen-doped graphene functionalized with ultralow Pt loading in an impactful *Z*-scheme flatform for photocatalytic hydrogen evolution, J. Mater. Chem. A **10**, 3330 (2022).

[33] B. Liu, M. Q. Long, M. Q. Cai, X. T. Hao, and J. L. Yang, Ferroelectric polarization in $CsPbI_3/CsSnI_3$ perovskite heterostructure, J. Phys. Chem. C **122**, 17820 (2018).

[34] X. X. Feng, B. Liu, M. Q. Long, M. Q. Cai, Y. Y. Peng, and J. L. Yang, Improving stability of lead halide perovskite via PbF_2 layer covering, J. Phys. Chem. Lett. **11**, 6266 (2020).

[35] G. Di Liberto, O. Fatale, and G. Pacchioni, Role of surface termination and quantum size in α-CsPbX_3 ($X = \mathrm{Cl, Br, I}$) 2D nanostructures for solar light harvesting, Phys. Chem. Chem. Phys. **23**, 3031 (2021).

[36] J. Hafner, *Ab-initio* simulations of materials using VASP: Density-functional theory and beyond, J. Comput. Chem. **29**, 2044 (2008).

[37] Q. L. Li, T. Song, Y. P. Zhang, Q. Wang, and Y. Yang, Boosting photocatalytic activity and stability of lead-free $Cs_3Bi_2Br_9$ perovskite nanocrystals via *in situ* growth on monolayer 2D $Ti_3C_2T_x$ *MX*ene for C–H bond oxidation, ACS Appl. Mater. Interfaces **13**, 27323 (2021).

[38] T. C. Leung, C. L. Kao, and W. S. Su, Relationship between surface dipole, work function and charge transfer: Some exceptions to an established rule, Phys. Rev. B **68**, 195408 (2003).

[39] A. Natan, Y. Zidon, Y. Shapira, and L. Kronik, Cooperative effects and dipole formation at semiconductor and self-assembled-monolayer interfaces, Phys. Rev. B **73**, 193310 (2006).

[40] A. Natan, L. Kronik, and Y. Shapira, Computing surface dipoles and potentials of self-assembled monolayers from first principles, Appl. Surf. Sci. **252**, 7608 (2006).

[41] L. Segev, A. Salomon, A. Natan, D. Cahen, and L. Kronik, Electronic structure of Si(111)-bound alkyl monolayers: Theory and experiment, Phys. Rev. B **74**, 165323 (2006).

[42] Y. H. Cao, Y. F. Li, J. W. He, C. X. Qian, Q. Zhang, J. T. Bai, and H. J. Feng, Asymmetric strain-introduced interface effect on the electronic and optical properties of the $CsPbI_3/SnS$ van der Waals heterostructure, Adv. Mater. Interfaces **6**, 1901330 (2019).

[43] M. Gajdoš, K. Hummer, G. Kresse, J. Furthmüller, and F. Bechstedt, Linear optical properties in the projector-augmented wave methodology, Phys. Rev. B **73**, 045112 (2006).

[44] Y.-Q. Zhao, L.-J. Wu, B. Liu, L.-Z. Wang, P.-B. He, and M.-Q. Cai, Tuning superior solar cell performance of carrier mobility and absorption in perovskite $CH_3NH_3GeCl_3$: A density functional calculations, J. Power Sources **313**, 96 (2016).

[45] See the Supplemental Material at http://link.aps.org/supplemental/10.1103/PhysRevApplied.18.054036 for [six figures and three tables. Figure S1 illustrates the calculated band structure of $Cs_3Bi_2Br_9$ bulk for (a) the HSE06 functional and (b) the PBE functional. Figure S2 illustrates the crystal structure of the $Cs_3Bi_2Br_9$ slab for three different surfaces. Figure S3 illustrates the energy-level diagrams of $Cs_3Bi_2Br_9$ and $Ti_3C_2T_2$ before contact states. Figure S4 illustrates the calculated band structure of the $Cs_3Bi_2Br_9$ surface for the PBE functional. Figure S5 illustrates the density of states of Bi, Br, and Ti atoms for (a) $Cs_3Bi_2Br_9/Ti_3C_2$, (b) $Cs_3Bi_2Br_9/Ti_3C_2F_2$, (c) $Cs_3Bi_2Br_9/Ti_3C_2Cl_2$, (d) $Cs_3Bi_2Br_9/Ti_3C_2O_2$, and (e) $Cs_3Bi_2Br_9/Ti_3C_2(OH)_2$. Figure S6 illustrates the plane-averaged charge-density difference, $\Delta\rho(z)$, and the charge-displacement curves of the $Cs_3Bi_2Br_9/Ti_3C_2$, $Cs_3Bi_2Br_9/Ti_3C_2F_2$, $Cs_3Bi_2Br_9/Ti_3C_2Cl_2$, and $Cs_3Bi_2Br_9/Ti_3C_2O_2$ heterostructures along the z direction. Table S1 lists the surface energies of the $Cs_3Bi_2Br_9$ slab for the three different surfaces. Table S2 lists the vertical interlamination spacing and minimum interface-bonding distance of the $Cs_3Bi_2Br_9/Ti_3C_2T_2$ heterostructures. Table S3 lists the binding energies of the $Cs_3Bi_2Br_9/Ti_3C_2T_2$ heterostructures].